Cosmic degeneracies – II. Structure formation in joint simulations of warm dark matter and $f(R)$ gravity

Marco Baldi[1,2,3]★ and Francisco Villaescusa-Navarro[4,5]

[1]*Dipartimento di Fisica e Astronomia, Alma Mater Studiorum Università di Bologna, viale Berti Pichat 6/2, I-40127 Bologna, Italy*

[2]*INAF – Osservatorio Astronomico di Bologna, via Ranzani 1, I-40127 Bologna, Italy*

[3]*INFN – Sezione di Bologna, viale Berti Pichat 6/2, I-40127 Bologna, Italy*

[4]*INAF – Osservatorio Astronomico di Trieste, via Tiepolo 11, I-34143 Trieste, Italy*

[5]*INFN – Sezione di Trieste, via Valerio 2, I-34127 Trieste, Italy*

ABSTRACT

We present for the first time the outcomes of a cosmological *N*-body simulation that simultaneously implements a warm dark matter (WDM) particle candidate and a modified gravitational interaction in the form of $f(R)$ gravity, and compare its results with the individual effects of these two independent extensions of the standard ΛCDM scenario, and with the reference cosmology itself. We consider a rather extreme value of the WDM particle mass ($m_{\mathrm{WDM}} = 0.4\,\mathrm{keV}$) and a single realization of $f(R)$ gravity with $|\bar{f}_{R0}| = 10^{-5}$, and we investigate the impact of these models and of their combination on a wide range of cosmological observables with the aim to identify possible observational degeneracies. Differently from the case of combining $f(R)$ gravity with massive neutrinos, we find that most of the considered observables do not show any significant degeneracy due to the fact that WDM and $f(R)$ gravity are characterized by individual observational signatures with a very different functional dependence on cosmic scales and halo masses. In particular, this is the case for the non-linear matter power spectrum in real space, for the halo and subhalo mass functions, for the halo density profiles and for the concentration–mass relation. However, other observables – like e.g. the halo bias – do show some level of degeneracy between the two models, while a very strong degeneracy is observed for the non-linear matter power spectrum in redshift space, for the density profiles of small cosmic voids, and for the voids abundance as a function of the void core density.

Key words: galaxies: formation – dark energy – dark matter – cosmology: theory.

1 INTRODUCTION

The presently accepted standard cosmological scenario – known as Λ cold dark matter (ΛCDM) – has been proved as an extremely successful model capable to explain numerous cosmological observations, from the statistical properties of the anisotropies in the cosmic microwave background (CMB; Planck Collaboration XIII 2016) to the clustering properties of galaxies or cosmic neutral hydrogen on large scales (Delubac et al. 2015; Alam et al. 2017). This model assumes that the observed accelerated expansion of the Universe (Riess et al. 1998; Schmidt et al. 1998; Perlmutter et al. 1999) is driven by a cosmological constant Λ whose value is set by observations, and that the dark matter that drives the growth of cosmic structures is *cold*, i.e. it has negligible thermal velocities at all redshifts.

Despite the spectacular success of the ΛCDM model, some of its predictions are in tension with observations on both large and small scales. In particular, a persisting tension has recently emerged between the best-fitting cosmological parameters obtained for a ΛCDM cosmology from CMB observations (Planck Collaboration XIII 2016) and a number of large-scale structure observations including weak gravitational lensing (Heymans et al. 2013; Hildebrandt et al. 2017), redshift-space distortions induced by the peculiar motion of galaxies (Blake et al. 2011; Reid et al. 2012; Simpson et al. 2016) or galaxy clusters (Vikhlinin et al. 2009), as well as from galaxy cluster counts (Planck Collaboration XXIV 2016). Furthermore a number of long-standing observational tensions at small scales are still persisting. Among these there are (i) the cusp-core problem: *N*-body simulations predict that the density profile of dark matter haloes exhibits a cusp in their cores, while from observations we know that some galaxies present a core in their density profile (Gilmore et al. 2007; Salucci et al. 2007; van Eymeren et al. 2009; Kuzio de Naray et al. 2010; Walker & Peñarrubia 2011). (ii) The missing satellite problem: the number of

satellites around Milky Way dark matter haloes from simulations is much larger than the number we observe (Klypin et al. 1999; Moore et al. 1999). (iii) The too-big-to-fail problem: the kinematic properties of the most massive subhaloes around Milky Way haloes from simulations are in strong tension with observations (Boylan-Kolchin, Bullock & Kaplinghat 2011, 2012).

In order to overcome these tensions and to alleviate the theoretical naturalness problems associated with the observed energy scale of the cosmological constant, several modifications of the standard ΛCDM cosmology have been proposed and investigated over the past decades. In particular, in the present work we will be focusing on warm dark matter (WDM) scenarios aiming to solve the small-scale issues of the standard model, and on modified gravity (MG) theories as possible alternative and more natural explanations for the observed accelerated cosmic expansion, also possibly providing new interpretations to the above-mentioned large-scale tensions.

Both these alternative cosmological scenarios have been widely investigated in the literature and their effects on a large number of observables have been tested and clarified. In particular, WDM models have been tested by numerous authors (see e.g. Colín, Avila-Reese & Valenzuela 2000; Avila-Reese et al. 2001; Bode, Ostriker & Turok 2001; Yoshida et al. 2003; Lovell, Eke, Frenk et al. 2012; Maccio et al. 2012; Schneider et al. 2012; Viel et al. 2012; Carucci et al. 2015; Maio & Viel 2015, and references therein) and their impact on the formation of structures at small scales has been compared with observations (Narayanan et al. 2000; Viel et al. 2005, 2013; Miranda & Maccio 2007; Markovic et al. 2011; Kennedy et al. 2014) thereby placing constraints on the viable WDM particle mass. Similarly, in more recent years MG cosmologies have attracted significant interest for their expected impact on structure formation and on the evolution of collapsed structures. In particular, the $f(R)$ gravity theory that will be discussed in the present work has been implemented in simulation codes of structure formation by several authors (Li et al. 2012; Puchwein, Baldi & Springel 2013; Llinares, Mota & Winther 2014) and a wide range of simulated observables within these MG scenarios have been obtained (just to mention some, see e.g. Jennings et al. 2012; Li, Zhao & Koyama 2012; Fontanot et al. 2013; Li et al. 2013; Arnold, Puchwein & Springel 2014, 2015; Cai et al. 2014; Hellwing et al. 2014; Cai, Padilla & Li 2015; Achitouv et al. 2016).

In the present work we aim to investigate the joint effects of these two independent modifications of the standard cosmological model, testing for possible observational degeneracies and quantifying the deviations that each model produces on the expected signatures of the other. This type of analysis has already been performed for the combination of $f(R)$ gravity theories with a non-negligible value of the total neutrino mass (Baldi et al. 2014) allowing us to identify a very strong degeneracy between these two classes of models. We will therefore proceed along the lines of Baldi et al. (2014) and explore the joint effects of $f(R)$ gravity and WDM particle candidates using high-resolution cosmological simulations. In doing so, we will considerably extend the range of observables under investigation with respect to Baldi et al. (2014) – which focused only on the matter power spectrum, halo mass function and halo bias – by including in our analysis also the subhalo mass function, halo density profiles and concentrations, as well as structural and statistical properties of cosmic voids.

This paper is organized as follows. In Section 2 we will provide a brief overview on the two physical models considered in this work, namely $f(R)$ gravity in Section 2.1 and WDM in Section 2.2. In Section 3 we will describe the numerical set-up adopted in the present work and the approaches employed for the identification of collapsed haloes and cosmic voids. In Section 4 we will illustrate the outcomes of our analysis on a wide range of cosmological observables. Finally, in Section 5 we will summarize our results and drive our conclusions.

2 THE COSMOLOGICAL MODELS

2.1 $f(R)$ gravity

Regarding possible modifications of the theory of gravity, as anticipated above, we will consider extensions to standard general relativity (GR) in the form of $f(R)$ gravity, which is by far the most widely studied class of MG scenarios, with a very extended literature devoted to the investigation of their impact on linear (Pogosian & Silvestri 2008; Hu et al. 2016) and non-linear structure formation (see e.g. Oyaizu, Lima & Hu 2008; Schmidt et al. 2009; Li et al. 2013; Puchwein, Baldi & Springel 2013; Llinares, Mota & Winther 2014).

$f(R)$ gravity is characterized by the action

$$S = \int d^4 x \sqrt{-g} \left(\frac{R + f(R)}{16\pi G} + \mathcal{L}_{\mathrm{m}} \right), \tag{1}$$

where the standard Einstein–Hilbert term R (with R being the Ricci scalar curvature) is replaced by $R + f(R)$. In equation (1), G is Newton's gravitational constant, g is the determinant of the metric tensor $g_{\mu\nu}$ and $\mathcal{L}_{\mathrm{m}}$ is the Lagrangian density of all matter fields. The model can be described by an additional scalar degree of freedom associated with the quantity $f_R \equiv df(R)/dR$. In the weak-field and quasi-static limit this scalar field obeys an independent dynamic equation (see e.g. Hu & Sawicki 2007):[1]

$$\nabla^2 f_R = \frac{1}{3} \left(\delta R - 8\pi G \delta \rho \right), \tag{2}$$

where δR and $\delta \rho$ are the relative perturbations in the scalar curvature and matter density, respectively.

A popular choice within all possible forms of the function $f(R)$ was proposed by Hu & Sawicki (2007):

$$f(R) = -m^2 \frac{c_1 \left(\frac{R}{m^2} \right)^n}{c_2 \left(\frac{R}{m^2} \right)^n + 1}, \tag{3}$$

where $m^2 \equiv H_0^2 \Omega_{\mathrm{M}}$ is a mass scale, while c_1, c_2 and n are non-negative constant free parameters of the model. The choice of equation (3) has the appealing feature of allowing us to recover with arbitrary precision the expansion history of a ΛCDM cosmology by choosing $c_1/c_2 = 6\Omega_\Lambda/\Omega_{\mathrm{M}}$ under the condition $c_2(R/m^2)^n \gg 1$, so that the scalar field f_R takes the approximate form

$$f_R \approx -n \frac{c_1}{c_2^2} \left(\frac{m^2}{R} \right)^{n+1}. \tag{4}$$

In this work we will only consider models with $n = 1$, which leaves c_2 as the only free parameter of the model. The latter can be also expressed in terms of the associated value of the mean scalar degree of freedom at the present epoch, $\bar{f}_{R0}$. As this convention has become the standard one in studies of $f(R)$ gravity models, we will also specify our cosmologies by their $\bar{f}_{R0}$ value.

In $f(R)$ models, the dynamical gravitational potential Φ (with which we denote the time–time metric perturbation; see e.g.

---

[1] We work in units where the speed of light is set to unity, $c = 1$.

equation 2 in Winther et al. 2015) obeys the equation (Hu & Sawicki 2007)

$$\nabla^2 \Phi = \frac{16\pi G}{3} a^2 \delta\rho - \frac{1}{6} a^2 \delta R, \quad (5)$$

which can be rewritten as

$$\nabla^2 \Phi = \nabla^2 \Phi_N - \frac{1}{2}\nabla^2 f_R, \quad (6)$$

where Φ_N is the standard Newtonian potential, so that the total gravitational force is governed by a modified potential $\Phi = \Phi_N - \frac{1}{2} f_R$ (while the lensing potential Ψ remains unchanged).

The resulting fifth force – proportional to ∇f_R – is Yukawa suppressed for scales larger than the Compton wavelength of the field:

$$\lambda_C = a^{-1}\sqrt{3\mathrm{d}f_R/\mathrm{d}R} = a^{-1}\sqrt{6|f_{R0}|\frac{\bar{R}_0^2}{R^3}}, \quad (7)$$

which for the particular choice of parameters adopted in this work is of the order of $\approx 7.7\,h^{-1}$ Mpc at the present epoch. Furthermore, as a consequence of the non-linear dependence of δR on the scalar degree of freedom f_R, the $f(R)$ gravity theory exhibits the so-called chameleon screening mechanism (Khoury & Weltman 2004), i.e. the property that the Compton wavelength shrinks (or equivalently the scalar field mass $m_{f_R} \sim 1/\lambda_C$ increases) in high-density regions of the universe, thereby confining the fifth-force propagation to arbitrarily short distances, which provides a way to evade Solar system constraints on gravity (see e.g. Bertotti, Iess & Tortora 2003; Will 2005; Lombriser 2014). A direct consequence of the chameleon screening is that collapsed structures of different masses will be generally in different screening regimes. In particular, a transition between the screened and unscreened regimes occurs at a mass $M_s \approx 10^{13}\,h^{-1}\,\mathrm{M}_\odot(|f_{R0}|/10^{-6})^{1.5}$ (see Schmidt 2010; Gronke, Mota & Winther 2015) where haloes with masses $M \gg M_s$ are fully screened, while haloes with masses $M \ll M_s$ are fully unscreened. For the models under investigation in the present work, the transition mass at $z = 0$ is of the order of $3 \times 10^{14}\,h^{-1}\,\mathrm{M}_\odot$.

MGmodels can be constrained by different types of observations based on the different phenomenological effects that they imprint on gravitating systems at different scales, from the local dynamics of the Solar system to the impact on the background expansion of the universe and large-scale structure (see e.g. Lombriser 2014, for an excellent recent review on observational constraints on chameleon MG theories). In particular, $f(R)$ gravity is already quite severely constrained by the structural and dynamical properties of small-scale structures, from the Solar system (see e.g. Hu & Sawicki 2007; Lombriser, Koyama & Li 2014) to dwarf galaxies (see e.g. Jain & VanderPlas 2011; Jain, Vikram & Sakstein 2013; Vikram et al. 2013), with upper limits on the background scalar amplitude $|f_{R0}|$ of 8×10^{-7} and 1×10^{-7}, respectively. Nonetheless, $f(R)$ gravity models with larger f_{R0} values still represent an interesting test bed for large-scale structure phenomenology, especially considering that simple extensions of the basic $f(R)$ scenario – as e.g. by allowing an effective decoupling of the scalar degree of freedom from ordinary baryonic matter – would evade such local bounds and would be mostly constrained by large-scale structure formation. In the present work we will consider $|f_{R0}| = 10^{-5}$, which is marginally consistent with most large-scale structure constraints still providing interesting phenomenology and – as we will see below – a non-trivial interplay with the effects of WDM.

For our simulations we will employ the MG-GADGET code (Puchwein et al. 2013) that consistently includes the effects of the modified potential and its associated chameleon screening mech-

anism and Yukawa suppression. The MG-GADGET code features a Newton–Gauss–Seidl iterative scheme to solve equation (2) for a generic density field produced by a set of discrete particles, and computes the total force experienced by each particle through equation (5) by including in the gravitational source term the curvature perturbation δR derived according to equation (2). We refer the interested reader to the MG-GADGET code paper for a more thorough presentation of the numerical implementation.

2.2 Warm dark matter

A possible way to solve both the cusp-core and missing satellite problems, while preserving the success of CDM on large scales, is to enable the possibility that dark matter has non-negligible thermal velocities. This is what is referred to by the term warm dark matter (WDM). In WDM models, the formation of haloes/subhaloes on scales smaller than the dark matter free-streaming length will be extremely suppressed, since only processes such as halo fragmentation may produce such objects. On the other hand, if dark matter has a non-zero temperature (i.e. thermal velocities are non-negligible), the dark matter phase space is finite, which implies that the density profile of haloes cannot be cuspy, but should exhibit an inner core. Thus, both the missing satellite and the cusp-core problems would be naturally alleviated by invoking non-negligible dark matter thermal velocities.

In terms of matter power spectrum, models with WDM will exhibit a cut-off on small scales, produced by the dark matter thermal velocities, that inhibits the matter clustering on scales smaller than the free-streaming length. The cut-off in the primordial density power spectrum can be expressed as a transfer function with the form (Bode et al. 2001)

$$T_{\mathrm{lin}}^2(k) \equiv P_{\mathrm{WDM}}(k)/P_{\Lambda\mathrm{CDM}}(k) = (1 + (\alpha k)^{2\nu})^{-10/\nu},$$
$$\alpha = 0.048\,h^{-1}\,\mathrm{Mpc}\left(\frac{1\,\mathrm{keV}}{m_{\mathrm{WDM}}}\right)^{\gamma_1}\left(\frac{\Omega_{\mathrm{WDM}}}{0.4}\right)^{\gamma_2}\left(\frac{h}{0.65}\right)^{\gamma_3},$$
$$(8)$$

with $\gamma_1 = 1.15$, $\gamma_2 = 0.15$, $\gamma_3 = 1.3$ and $\nu = 1.2$. Other forms of the linear power suppression have been found in the literature (see e.g. Hansen et al. 2002) with a similar qualitative behaviour.

This signature can be used to put constraints on the mass (or magnitude of the thermal velocities) of the WDM particles. The tightest constraints to date arise from measurements of the amplitude and shape of the Lyα power spectrum, resulting in a 2σ limit of $m_{\mathrm{WDM}} \geq 3.3$ keV (Viel et al. 2013). Constraints from weak lensing (Inoue et al. 2015) and high-redshift galaxy counts (Schultz et al. 2014), although less tight ($m_{\mathrm{WDM}} > 1.3$ keV), are also consistent with this bound.

We emphasize that the above constraints have been derived for ΛWDM models, where CDM is simply replaced by WDM. The purpose of this paper is to investigate the statistical properties of matter and haloes, subhaloes and voids, in cosmologies with both MG and WDM, for which the above quoted limits may no longer apply.

3 THE SIMULATIONS

We perform four high-resolution simulations for four different cosmological models characterized by different laws of gravity and dark matter particle mass.

As a reference model, we consider a standard ΛCDM scenario, i.e. a model where gravity is governed by standard GR and the dark matter particle mass is formally infinite, in the sense that thermal

Table 1. The set of cosmological parameters adopted in the present work, consistent with the latest results of the Planck Collaboration (Planck Collaboration XVI 2014). Here n_s is the spectral index of primordial density perturbations, while $\mathcal{A}_s$ is the amplitude of scalar perturbations at the redshift of the CMB.

Parameter	Value
H_0	$67.1\,\mathrm{km\,s^{-1}\,Mpc^{-1}}$
Ω_M	0.3175
Ω_{DE}	0.6825
Ω_b	0.049
$\mathcal{A}_s$	2.215×10^{-9}
n_s	0.966

velocities are negligible and the linear matter power spectrum does not exhibit any cut-off on small scales.

For the same dark matter particle mass we investigate also the case where gravity is described by the $f(R)$ theory described above in Section 2.1 for a scalar amplitude at $z = 0$ of $|\bar{f}_{R0}| = 10^{-5}$. In our numerical integrations of $f(R)$ gravity we assumed the background expansion history to exactly match the ΛCDM one.

In addition, we will consider two cosmological models characterized by these two different theories of gravity (GR and $|\bar{f}_{R0}| = 10^{-5}$) and by a dark matter particle mass of 0.4 keV, thereby corresponding to a WDM candidate with a 'very warm' temperature. Although being strongly disfavoured by the Lyman α, weak lensing, and number counts observational constraints already mentioned above (Viel et al. 2013; Schultz et al. 2014; Inoue et al. 2015), we consider such a low value of the dark matter particle mass in order to more easily highlight its effects on the various observables we will consider in the present work, as the thermal cut-off for such low mass is already significant at scales that are more easily resolved by our simulations. Therefore, our set-up will provide a very prominent example of how the degeneracy with the underlying theory of gravity might affect some observational features that are usually employed to derive constraints on the dark matter particle mass. Furthermore, this value corresponds to the most extreme value considered in the recent work by Yang et al. (2015) about the impact of WDM on the properties of cosmic voids to which we aim comparing some of our results. The corresponding free-streaming length for this model is given by (Viel et al. 2013)

$$k_{FS} \sim 15.6 \frac{h}{\mathrm{Mpc}} \left(\frac{m_{WDM}}{1\,\mathrm{keV}} \right)^{4/3} \left(\frac{0.12}{\Omega_{WDM} h^2} \right)^{1/3}, \qquad (9)$$

which for $m_{WDM} = 0.4\,\mathrm{keV}$ is $k_{FS} \sim 4.3\,h\,\mathrm{Mpc}^{-1}$. The characteristic mass scale below which haloes abundance is expected to be suppressed is (Bode et al. 2001)

$$M = 10^{10}\,h^{-1}\mathrm{M}_\odot \left(\frac{\Omega_{WDM}}{0.3} \right)^{1.45} \left(\frac{h}{0.65} \right)^{3.9} \left(\frac{\mathrm{keV}}{m_{WDM}} \right)^{3.45}, \quad (10)$$

i.e. $\sim 3 \times 10^{11}\,h^{-1}\,\mathrm{M}_\odot$ for a model with 0.4 keV WDM.

Our simulations evolve a set of 512^3 particles in a periodic cosmological box of 100 comoving h^{-1} Mpc aside, with a mass resolution of $m \approx 6.3 \times 10^8\,\mathrm{M}_\odot\,h^{-1}$ and a gravitational softening of $\epsilon_g = 6\,\mathrm{kpc}\,h^{-1}$. All simulations share the same cosmological parameters (summarized in Table 1, consistent with *Planck* cosmological constraints; Planck Collaboration XIII 2016) and the same background expansion history since both WDM and $f(R)$ gravity (for the Hu & Sawicki 2007 set-up adopted in the present work) do not appreciably affect the background evolution of the universe.

For the WDM simulations we imprint the thermal cut-off described by equation (9) on to the primordial power spectrum when generating the initial conditions, which are produced by displacing particles from a regular Cartesian grid according to Zel'dovich approximation (Zel'dovich 1970) at a starting redshift of $z = 127$. On top of the peculiar velocities, we add to the particles thermal velocities whose magnitude is randomly drawn from the WDM momentum distribution. The orientation of the thermal velocity vector is taken randomly within the sphere.

It is a well-known fact that standard *N*-body simulations of WDM suffer of numerical artefacts such as the formation of spurious haloes along the filaments of the cosmic web (Wang & White 2007). Such artificial fragmentation then results in a population of small haloes that do not correspond to real physical objects. Numerical approaches to overcome this problem have been discussed e.g. by Angulo, Hahn & Abel (2013). We do not employ such alternative approaches as we are mostly interested in the degeneracy with the underlying theory of gravity and a possible increase of the abundance of low-mass haloes due to artificial fragmentation would simply make our results more conservative.

Because of limitations of computational resources and the highly demanding integration of the combined simulation we stop our runs at $z = 0.25$ and we will perform all our analysis at this redshift. This is not expected to affect significantly the main conclusions of our investigation.

3.1 The halo catalogues

For all our four simulations we identify particle groups through a Friends-of-Friends (FoF) algorithm (Davis et al. 1985) with a linking length of 0.2 times the mean interparticle separation, and store groups composed by at least 32 particles. On top of these catalogues we run the SUBFIND algorithm (Springel et al. 2001) to identify gravitationally bound substructures of each FoF group, and store haloes with at least 20 particles for which we compute spherical overdensity quantities as e.g. the virial mass M_{200} and virial radius R_{200} referred to the critical density of the universe, defined by the relation

$$\frac{4\pi}{3} R_{200}^3 \Delta \rho_{crit} = M_{200}, \qquad (11)$$

with $\Delta = 200$ and $\rho_{crit} = 3H^2/(8\pi G)$.

For our analysis we will only use haloes whose main substructure has a virial mass M_{200} in the range $[10^{11}, 10^{14}]\,\mathrm{M}_\odot\,h^{-1}$: for higher halo masses the number of haloes is too low to provide robust statistical conclusions, while lower masses are poorly resolved. With such catalogues at hand we will investigate the effects of WDM and of its combination with $f(R)$ gravity on a number of statistical and structural properties of the halo populations arising in the various cosmologies, as described below in Section 4.2.

3.2 Voids identification and selection

We identify cosmic voids in our simulations suite by means of the publicly available void finder VIDE (Sutter et al. 2015) by running it on a random subsample of the dark matter particle distribution extracted from the $z = 0.25$ snapshot of the various runs. VIDE is based on the ZOBOV algorithm (Neyrinck 2008), which allows to identify wells in the density field produced by a set of points. This is done by means of a Voronoi tessellation scheme that associates a cell to each tracer of the density field and subsequently identifies local density minima among these cells by looking for cells with a larger

Voronoi volume than all surrounding cells. By joining together the Voronoi cells around a local density minimum based on the watershed transform algorithm (see Platen, van de Weygaert & Jones 2007), a hierarchy in the structures of the identified voids is naturally obtained. Finally, the VIDE toolkit elaborates on the void catalogue obtained by ZOBOV by performing various possible selections of the void sample as e.g. different cuts on the void density contrast or on the void central overdensity.

For our analysis we will consider only voids with a central density below 20 per cent of the mean density of the universe and with a density contrast between the most underdense particle of the void and the void boundary no lower than 1.57, corresponding to a probability that the void arises from Poisson noise below ∼5 per cent (see again Neyrinck 2008).

A standard quantity to characterize cosmic voids and study their relative abundance is given by their effective radius $R_{\rm eff}$, defined from the Voronoi volume of the void as the radius of a sphere having the same volume as the void:

$$V_{\rm VOID} \equiv \sum_{i=1}^{N} V_i^p = \frac{4}{3}\pi R_{\rm eff}^3. \tag{12}$$

However, following the discussion presented in Yang et al. (2015), for the analysis presented in this work it is more convenient to characterize voids based on their core density, defined as the density of the most underdense Voronoi cell of each void. Such quantity will be employed in Section 4.3.1 below to characterize the abundance of voids in the different cosmologies under investigation.

4 RESULTS

We now present the main outcomes of our simulations. The various observables that will be discussed in this section have been extracted from the simulations snapshots using standard and well-tested numerical pipelines that are routinely employed for the analysis of cosmological simulations, and are presented in a very standard form. Therefore, we will not describe very extensively these procedures, the novelty of the present work being in the cosmological models investigated rather than on the analysis performed. We will focus on the statistical and structural properties of both dark matter haloes and cosmic voids.

A priori, we can expect that the total effect of the two combined models will be given by the separate effects of each of the two (i.e. WDM and $f(R)$ gravity on their own) plus a further contribution arising from their coupling, where by coupling we mean the fact that each model acts on a distribution of matter that is simultaneously modified by the other. As the effect of the coupling is expected to be non-trivial and act at all scales, it is hard to get any physical insight to the joint effects of the two models beyond the naive assumption that the coupling be small compared to the individual effects. Under such assumption, which as we will see below does not seem to be valid for all observables and at all scales, one can expect that the combined model will result in a simple superposition of the individual effects on the various observables. We notice however that analytic tools such as the halo model can be used to get some physical insight (Mead et al. 2016) and to predict the matter power spectrum in the fully non-linear regime.

4.1 Large-scale matter distribution

In Fig. 1 we show density slices extracted from the $z = 0.25$ snapshot of our simulations at different scales, namely $100\,h^{-1}$ Mpc (left-

hand column), $25\,h^{-1}$ Mpc (middle column) and $8\,h^{-1}$ Mpc (right-hand column), the latter being centred on the most massive halo identified by our halo finding procedure. As one can see from the figure, the shape of the large-scale structures remains the same in all cosmologies as a consequence of having used the same random realization of the density power spectrum in the initial conditions. Nonetheless, some differences in the abundance of substructures and in the concentration of the density peaks among the models can already be observed by eye. In particular, the abundance of small haloes appears substantially suppressed in the WDM runs.

4.1.1 The matter power spectrum

For all the simulations presented above we have computed the matter power spectrum at $z = 0.25$ through a Cloud-in-Cell mass assignment to a Cartesian grid with 768^3 nodes, thereby spanning the range of Fourier modes between $k_0 = 0.06\,h\,{\rm Mpc}^{-1}$ and the Nyquist frequency of $k_{\rm Ny} \approx 24\,h\,{\rm Mpc}^{-1}$. In Fig. 2 we show the ratio of the non-linear matter power spectrum at $z = 0.25$ to the standard cosmological scenario in the various models under investigation. As one can see from the plot, the WDM simulation within standard GR (solid red curve with open squares) shows the expected suppression of power at small scales, with deviations from the standard ΛCDM case starting at the cut-off scale $k_{\rm c} \approx 2\,h\,{\rm Mpc}^{-1}$. As a reference, we overplot as a dashed line the result of the non-linear fitting function provided by Viel et al. (2012):

$$T_{\rm nl}^2(k) \equiv P_{\rm WDM}(k)/P_{\rm \Lambda CDM}(k) = (1 + (\alpha\,k)^{\nu l})^{-s/\nu},$$

$$\alpha(m_{\rm WDM}, z) = 0.0476 \left(\frac{1{\rm keV}}{m_{\rm WDM}}\right)^{1.85} \left(\frac{1+z}{2}\right)^{1.3} h^{-1}{\rm Mpc}, \tag{13}$$

where we have used the values $\nu = 3$, $l = 0.8$ and $s = 0.2$ for the fitting parameters. As the figure shows, this analytical formula provides an excellent fit to the power suppression in the standard GR case. The dotted line displays the linear prediction provided by equation (9).

The $f(R)$ simulation for the case of CDM particles (solid green curve with triangles) gives rise to the expected scale-dependent power enhancement due to the action of the fifth force associated with the extra scalar degree of freedom f_R. This is consistent with a number of previous works and in particular with the outcomes of the code comparison project for $f(R)$ gravity cosmologies presented in Winther et al. (2015). The dotted line displays the linear prediction obtained with the Boltzmann code EFTCAMB[2] (Hu et al. 2014).

When we consider the combined simulation for a WDM particle with mass $m_{\rm WDM} = 0.4\,{\rm keV}$ and $f(R)$ gravity (solid blue curve with diamonds), we find (quite expectedly) that at large scales no significant difference appears with respect to the CDM–$f(R)$ case, while at scales below the cut-off $k_{\rm c}$ the power is suppressed compared to the CDM case. This is qualitatively expected, but the present work provides the first quantitative determination of the power suppression due to WDM in the context of an MG cosmological model. In particular, it is remarkable to notice that the non-linear suppression relative to the CDM model within $f(R)$ gravity shows the same shape and amplitude that is found for the GR case: the blue dashed curve in Fig. 2 – which represents the suppression obtained by applying the best-fitting suppression function from equation (13) for the GR case to the $f(R)$–CDM simulation – very well captures the power spectrum ratio computed from the simulations. This result appears to be consistent with the picture where perturbations with scales

---

[2] http://eftcamb.org
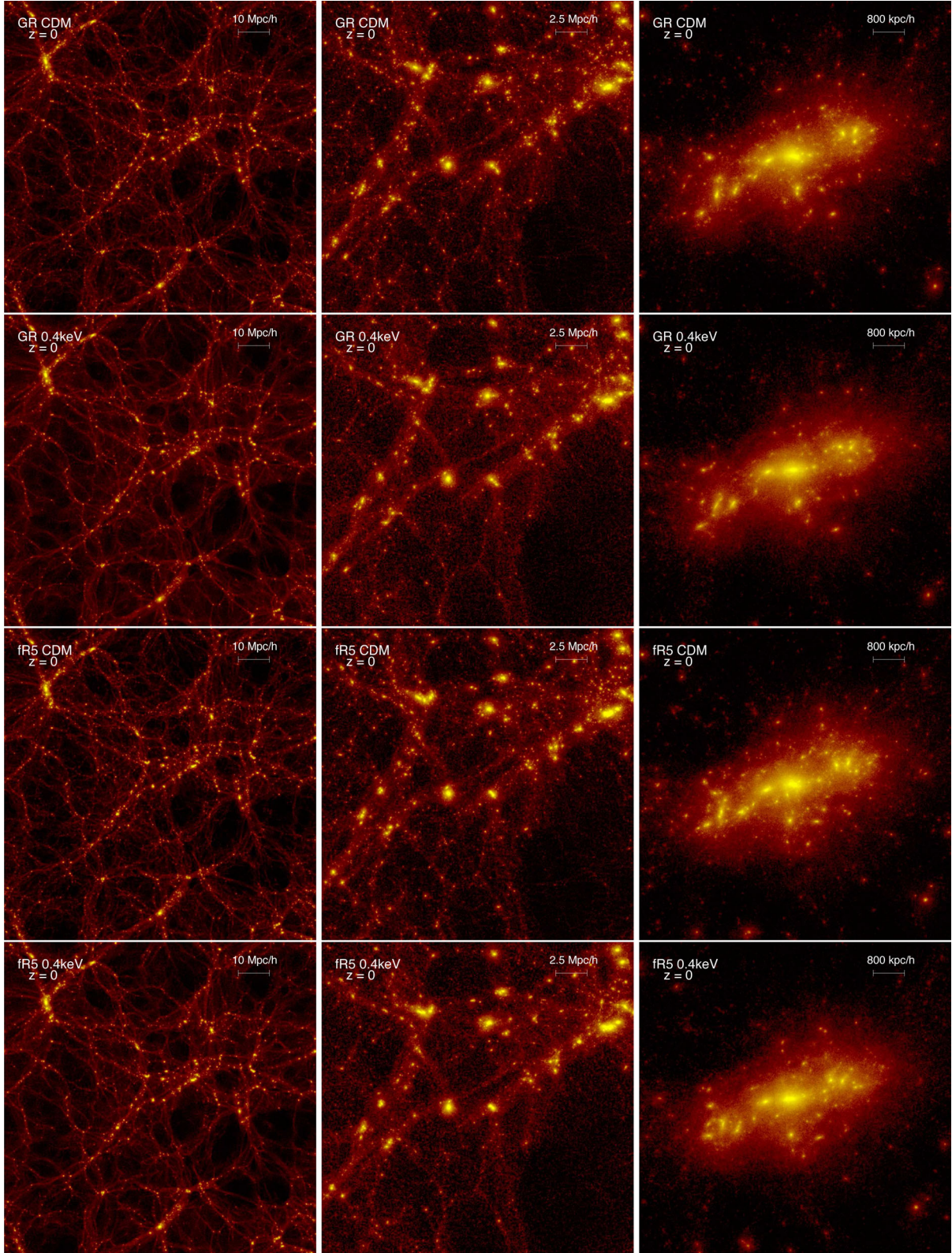
Figure 1. Density slices through the $z = 0.25$ snapshots of our simulations at various scales, as indicated in the labels.

larger than the WDM free-streaming length are the only subject to collapse, irrespective of the underlying theory of gravity. This is because the cut-off in the matter power spectrum is already in place at very high redshift, when MG is expected to have no effect due to the screening mechanism being working at all scales as a consequence of the high mean cosmic density. The subsequent faster growth of density perturbations dictated by the fifth force of MG for those regions of the universe where the latter becomes unscreened
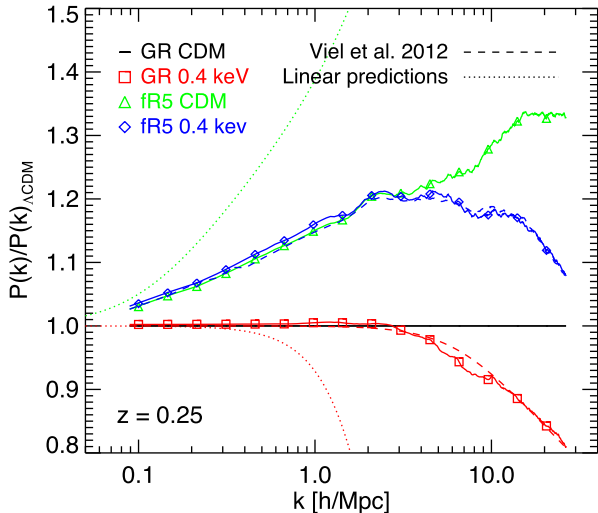
Figure 2. The ratio between the non-linear matter power spectrum to the reference non-linear power spectrum of ΛCDM model for the different cosmologies under investigation. The dotted curves show the linear-to-linear predictions obtained by numerical integration with EFTCAMB (Hu et al. 2014) for the $f(R)$ gravity case and by applying the transfer function of equation (9) to the linear ΛCDM power spectrum for the case of WDM. The red and blue dashed curves instead display the results of applying the fitting formula of Viel et al. (2012) for the WDM non-linear transfer function to the GR and $f(R)$ power spectrum extracted from the simulations, respectively: remarkably, the agreement with the results of the combined $f(R)$–WDM simulation is very good at all scales.

will then enhance the power on scales where seed fluctuations have survived, but will not be able to generate new structures beyond the free-streaming scale.

We have also computed the monopole of the matter power spectrum in redshift space at $z = 0.25$ for the four different models we investigate in this work. We move the particles from real space to redshift space using the distant observer approximation. We obtain three different realizations in redshift space by using the peculiar velocities of the particles along the three different Cartesian axes. The monopole in redshift space is obtained by averaging over the results from each realization. In Fig. 3 we show the results.

The upper panel of Fig. 3 displays the matter monopole in redshift space, normalized by the monopole of the ΛCDM model. Differences among all models are much smaller in redshift space than in real space. All models appear now consistent with the standard ΛCDM scenario within 5 per cent for large scales ($k \lesssim 2\,h\,\mathrm{Mpc}^{-1}$), thereby making their signatures hardly detectable. The model with MG and CDM is degenerate with ΛCDM at the ∼5 per cent level also at smaller scales. On the other hand, the models with WDM exhibit a suppression of power on small scales, with respect to their CDM counterparts. We find that the wavenumber were the cut-off shows up in the WDM models depends on whether the model is with GR or MG.

In the bottom panel of Fig. 3 we plot the ratio between the monopoles in redshift- and real space for the four different models. As can be seen, there is a clear distinction between models with GR and MG, since the shape and amplitude of the ratio are different on small scales. On the other hand, WDM does not seem to produce any effect on the monopoles ratio. On large scales, the monopoles ratio is expected to approach the value

$$\lim_{k \to 0} \frac{P^s(k)}{P^r(k)} = 1 + \frac{2}{3}\beta + \frac{1}{5}\beta^2, \qquad (14)$$
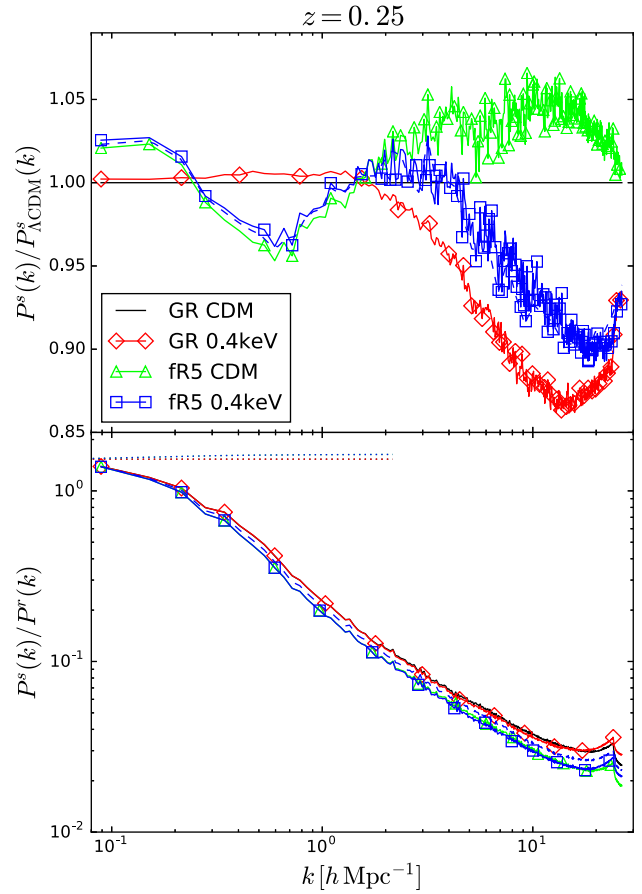
Figure 3. Upper panel: monopole of the matter power spectrum in redshift space normalized by the monopole of the ΛCDM model. Lower panel: ratio between the monopoles in redshift- and real space for the four different models. All results are shown at $z = 0.25$. The dashed blue curve shows the simple superposition of the relative deviation from ΛCDM of the two separate simulations. The dotted lines in the bottom panel show the prediction by linear theory.

where the redshift-space distortion parameter is $\beta = f(z)/b$, with $f(z)$ being the linear growth factor and b is the bias (in this case $b = 1$). The dotted lines in that panel shows the above Kaiser limit; we compute the growth rate of the models with MG using EFTCAMB. As expected the results of our simulations do not reach the Kaiser limit. This is expected given the scales our simulations can probe.

4.1.2 The halo bias

We have also investigated the clustering properties of dark matter haloes in the different models using the halo bias as our cosmological statistics. We have computed for each model the halo bias as the ratio between the halo–matter cross-power spectrum to the matter autopower spectrum. We have used this definition of halo bias to avoid stochasticity. Results are shown in Fig. 4.

Unfortunately, our simulation boxes are not large enough to allow us to explore the linear bias and whether any of these models exhibit a scale-dependent bias on large scales. We find that models with WDM present a higher amplitude of the halo bias than their CDM counterparts, irrespective of the underlying gravity model. This is the expected effect of WDM (Dunstan et al. 2011; Maccio et al. 2012): suppressing the abundance of low-mass haloes and therefore enhancing the clustering of haloes of all masses.
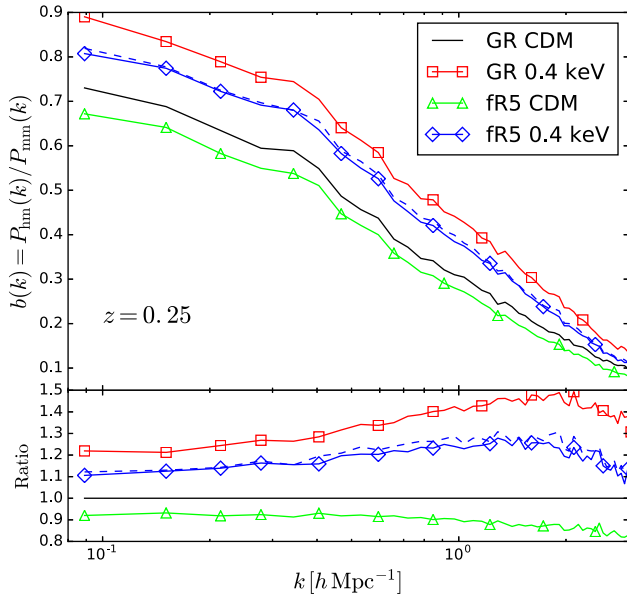
Figure 4. Halo bias at $z = 0.25$ in real space. Upper panels show the halo bias, computed as the ratio of the halo–matter cross-power spectrum over the matter autopower spectrum for the different models, as indicated in the legend. The bottom panel displays the halo bias normalized by the results of the ΛCDM cosmology. The dashed blue curve shows the simple superposition of the relative deviation from ΛCDM of the two separate simulations.

Nonetheless, the halo bias of the MG models is systematically lower than the one of the standard GR models by ∼10 per cent, which suggests that a stronger modification of gravity may completely balance the bias enhancement due to WDM, thereby giving rise to another observational degeneracy. The bottom panel of Fig. 4 shows the halo bias of the different models normalized by the results of the ΛCDM model. We find that on the largest scales the relative differences among the various models are almost scale independent.

An extended sampling of the $f(R)$ parameter space – which goes beyond the scope of the present work – would be required in order to confirm this speculation and identify the combination of parameters giving rise to a maximal degeneracy.

4.2 Statistical and structural properties of dark matter haloes

4.2.1 Halo mass function

We compute the differential halo mass function of all our cosmologies as the number of haloes identified by the SUBFIND algorithm having a virial mass M_{200} (see above) falling within 12 logarithmically equispaced mass bins ranging between 10^{11} and 10^{14} M$_\odot$ h^{-1}. In Fig. 5 we display the ratio of the abundance computed in each bin to the fiducial case represented by the ΛCDM cosmology.

As expected, the WDM model (shown as red open squares in the plot) results in a strong suppression of the abundance of small haloes with a reduction of ≈40 per cent of objects at the smallest mass side of our considered interval. At larger masses the halo abundance of the WDM cosmology recovers the ΛCDM expectation within statistical errors, displayed as the grey-shaded area in Fig. 5 and corresponding to the Poissonian error in each bin.

The $f(R)$ cosmology with CDM particles (blue open diamonds) shows on the contrary a mass-dependent enhancement of the abundance of haloes that becomes more pronounced for larger halo masses, reaching a ≈35 per cent increased halo abundance at the
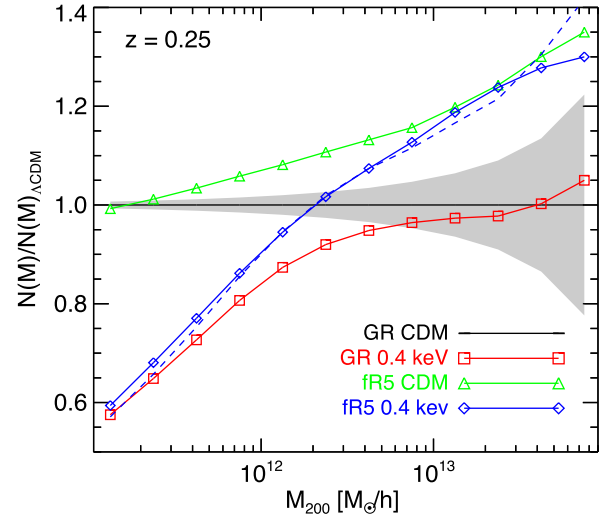
Figure 5. The halo mass function for the three cosmologies under investigation. The grey-shaded region represents the Poissonian error propagated to the counts ratio based on the number of haloes in each bin. The dashed blue curve shows the simple superposition of the relative deviation from ΛCDM of the two separate simulations: also in this case this simple combination reproduces extremely well the results of the combined simulation.

largest mass available to our halo sample. This is also an expected result and fully consistent with the outcomes of several previous works (as e.g. Li et al. 2012; Lombriser et al. 2013; Puchwein et al. 2013; Winther et al. 2015; Achitouv et al. 2016, just to mention some).

By comparing these first two simulations it appears already clear that no degeneracy between WDM and $f(R)$ gravity is to be expected for an observable as the halo mass function, since the two scenarios give rise to the opposite mass dependence of the deviation from the standard cosmological scenario. This is confirmed by directly checking the combined simulation (green open triangles) that shows how the small-mass suppression and the large-mass enhancement both persist in the combined halo mass function. Furthermore, the blue dashed curve obtained by simply combining the relative deviations of the two separate models reproduces very well the results of the combined simulation over the whole mass range, confirming that the effects of WDM and $f(R)$ gravity act in an almost independent way on the abundance of collapsed structures. Therefore, the combination of WDM and $f(R)$ gravity is expected to enhance the signal of a mismatch between the detected abundance of haloes at large and small masses.

4.2.2 Subhalo mass function

We also compute – for all the cosmologies under investigation – the subhalo mass function, defined as the abundance of substructures of mass M_{sub} that are gravitationally bound to a main halo of virial mass, M_{200}, as a function of the mass ratio M_{sub}/M_{200}. The results are displayed in Fig. 6 with the same colour- and symbol coding of the previous figures.

As one can see from the plot, the WDM case shows the expected suppression of the abundance of substructures, with about 25–40 per cent fewer subhaloes compared to ΛCDM for a mass fraction M_{sub}/M_{200} below 10^{-2}. The effect is significant when compared to the statistical error due to Poisson noise, which is represented in the plot by the grey-shaded region.
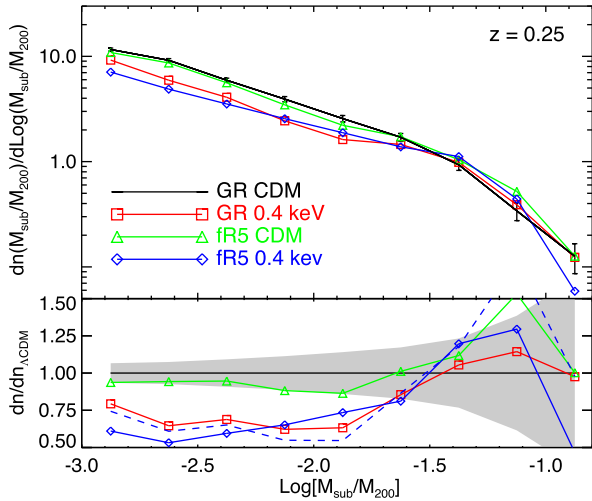
Figure 6. The subhalo mass function for the three cosmologies under investigation. The grey-shaded region represents the Poissonian error propagated to the counts ratio based on the number of subhaloes in each bin. The blue dashed curve shows the simple combination of the deviations obtained from the separate simulations of WDM and $f(R)$ gravity.

This suppression does not appear to be significantly modified when moving from GR to $f(R)$ as the underlying theory of gravity. In fact, the combined simulation shows approximately the same behaviour as the GR–WDM run. On the contrary, the $f(R)$–CDM simulation is found to be consistent with the standard scenario within statistical errors, even though a qualitatively similar trend to the WDM case is also observed, with a suppression of the subhalo abundance at the low-mass end and a corresponding enhancement at the high-mass end. Therefore, a stronger modification of gravity or a larger value of the WDM particle mass may be expected to determine a similar observational signal (both in shape and amplitude) in the subhalo mass function, thereby giving rise to a different type of degeneracy since the same detected signature could be ascribed to both phenomena, or to their combination.

Therefore, also for the case of the abundance of bound substructures within virialized haloes no significant degeneracy is found between the effects of a WDM particle and a modified theory of gravity in the form of $f(R)$, at least for the magnitude of the background scalar value $f_{R0} = -1 \times 10^{-5}$ considered in the present work. As in previous figures, the blue dashed curve shows the result of the simple combination of the deviations from ΛCDM obtained in the two separate simulations.

4.2.3 Halo density profiles

For each of the 12 mass bins employed to compute the differential halo mass function discussed above we have computed the average density profiles of up to 1000 haloes. This means that we have computed the mass density in a set of 30 logarithmic radial shells centred on the most bound particle of a halo for a random sample of haloes belonging to each mass bin, and then stacked these density profiles after rescaling the individual radial coordinates in units of the halo virial radius R_{200} to obtain an average profile for each bin. For those bins not reaching 1000 members we have performed the stacking using all the available members.

All the profiles, independently on the mass bin and on the cosmological model, have then been normalized to unity at the virial radius and we show the ratio of these profiles to the ΛCDM cosmology in

Fig. 7 for four out of the 12 available mass bins. The grey-shaded areas in the plot represent the 2σ confidence limits based on the standard deviation of the mean density profiles computed through a bootstrap resampling technique with 1000 resamples of the 1000 individual profiles.

As one can see in the plots, the WDM realization for a standard GR theory of gravity (red open squares) always results in shallower density profiles with a significant suppression of the central over-density and a lower profile slope, even though the effect is – as expected – more pronounced for the lowest mass bin and progressively decreases for higher mass haloes. In particular, for the largest masses available to our sample the profile is marginally consistent with the standard cosmological result at $\approx 2\sigma$. This is the very well-known effect of the thermal cut-off in the primordial density power spectrum, which determines the formation of cored density profiles for low-mass haloes and of progressively steeper profiles for increasing halo mass (Villaescusa-Navarro & Dalal 2011; Maccio et al. 2012).

On the contrary, the CDM realization for $f(R)$ gravity (green open triangles) shows a more complicated modulation of the deviation with respect to the standard model as a function of the halo mass. More specifically, while the profiles are completely unaffected at the highest mass bin displayed in the plots – as a consequence of the screening of the fifth force – for intermediate masses the effect of the modification of gravity results in a significant steepening of the profiles with up to a 50 per cent enhancement of the central overdensity for haloes of mass ≈ 1–$2 \times 10^{13}\,\mathrm{M_\odot}\,h^{-1}$, while at smaller masses we can observe an inversion of the effect, with galactic-sized haloes ($\approx 10^{12}\,\mathrm{M_\odot}$) being again consistent with ΛCDM while less massive haloes show a moderate shallowing of their inner profile. This behaviour is consistent with the effects of the chameleon screening mechanism that characterizes $f(R)$ gravity, with the most massive haloes being fully screened due to their deep potential wells, and the lowest mass haloes having formed and virialized at earlier epochs when the higher average cosmic density significantly suppresses the scalar fifth force.

It is particularly interesting then to test the outcomes of the combined WDM–$f(R)$ simulation (open blue diamonds) where the interplay between these opposite effects and their different dependence on the host halo mass might give rise to characteristic observational signatures. In particular, we find (quite surprisingly) that the shallowing of the density profiles for the low-mass haloes displayed in the top panels of Fig. 7 is somewhat enhanced in $f(R)$ gravity compared to standard GR, and this enhanced suppression goes beyond the simple superposition of the two separate effects shown by the blue dashed curve. On the contrary, for group-sized haloes (bottom left-hand panel in the figure) the effect of the fifth force overcomes the suppression due to WDM and the resulting density profiles are steeper than in the standard cosmological scenario, even though with a weaker enhancement of the central overdensity as compared to the CDM case, and to the simple superposition of the two separate effects. Finally, for the most massive haloes considered in our analysis the effect of the fifth force seems to be completely absent (due to the chameleon screening, as discussed above) and the combined model appears fully consistent with the WDM result in standard GR.

4.2.4 Concentrations

For each halo in our sample we have computed the concentration using two different methods that we will compare here for the first
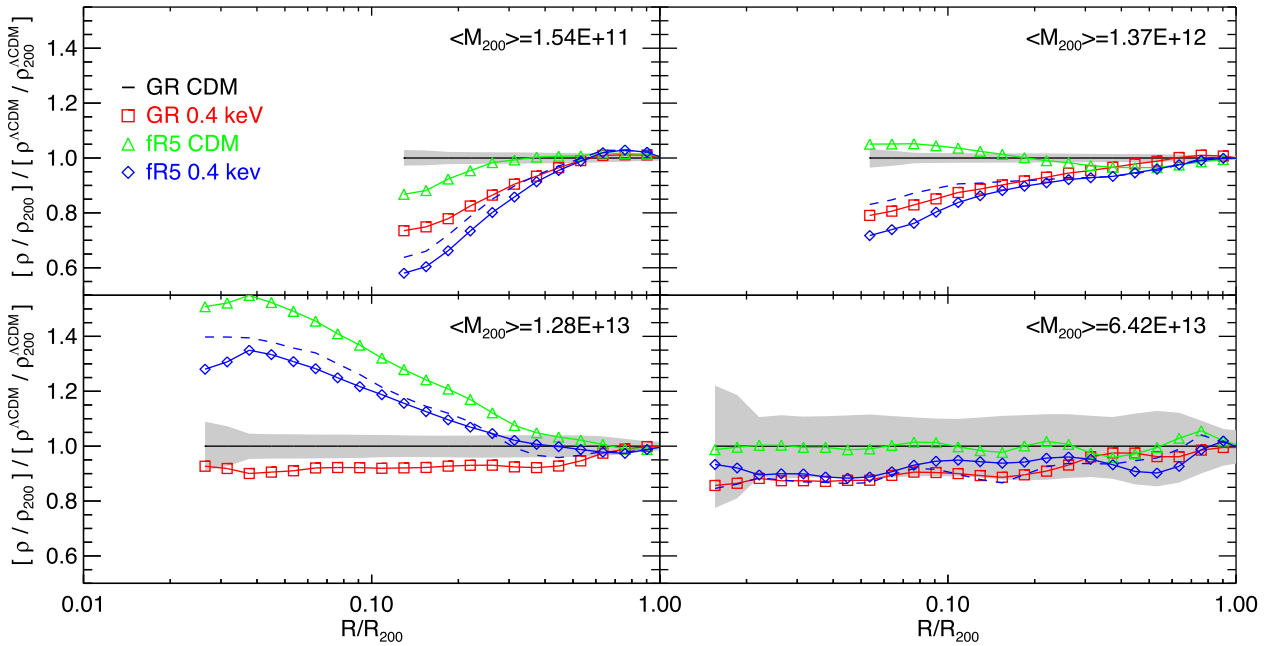
Figure 7. The ratio of the stacked halo density profiles to the fiducial GR+CDM cosmology for about 1000 haloes within four out of the 12 mass bins considered for the halo mass function and concentration analysis. The grey-shaded area represents a 2σ uncertainty on the stacked profile based on a bootstrap procedure. As in previous figures, the blue dashed curve represents the result of simply combining the deviations from the standard case of the two separate WDM and $f(R)$ simulations. In this case, however, such simple superposition of effects does not always reproduce the results of the combined simulation.

time for the case of non-standard gravity scenarios. One way to compute halo concentrations (which we will refer to as c^*) follows the approach described in Springel et al. (2008) by exploiting the relation

$$\frac{200}{3} \frac{c^{*3}}{\ln(1+c^*) - c^*/(1+c^*)} = 7.213\delta_V, \qquad (15)$$

where δ_V is defined as

$$\delta_V = 2\left(\frac{V_{\max}}{H_0 r_{\max}}\right)^2, \qquad (16)$$

with $V_{\max}$ and $r_{\max}$ being the maximum rotational velocity of the halo and the radius at which this velocity peak is located, respectively. Both quantities have been computed in all models based only on the gravitational potential associated with the matter density profile, therefore neglecting the effect of the additional fifth force. This approach to compute halo concentrations has already been employed in the context of $f(R)$ MG theories by Arnold, Springel & Puchwein (2016) for a small set of very well resolved Milky Way-sized haloes (by means of a set of zoomed high-resolution simulations) and compared with the results obtained from fitting the individual density profiles with a Navarro–Frenk–White (NFW; Navarro, Frenk & White 1997) shape. In our set-up we have a much poorer resolution than in the simulations of Arnold et al. (2016) but a significantly larger statistics. We can therefore repeat the comparison on a statistically significant sample of dark matter haloes by performing – as a second independent method to compute the concentration that we will refer to as c – a one-parameter fitting of an NFW shape for the individual profiles of all the 1000 randomly selected haloes used to compute the stacked density profiles discussed in the previous section.
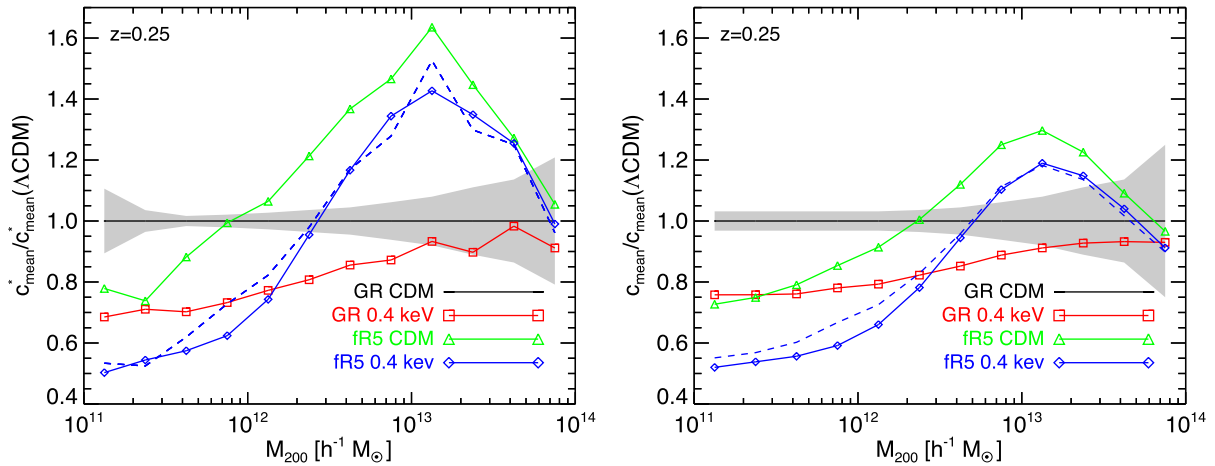
In Fig. 8 we show the ratio of the concentration–mass relation computed with these two different methods in the left- and right-hand panels, respectively, for all the cosmologies under investiga-

tion. The grey-shaded areas represent the 2σ confidence regions based on the Poisson errors on the mean for each mass bin.

As one can see from the two plots, the qualitative deviation from ΛCDM as a function of halo mass is consistent between the two methods, even though for the $f(R)$ gravity models the results are quantitatively different at intermediate masses. Such difference can be explained as a result of neglecting the effect of the fifth force on the relation between the density and velocity profiles encoded by equation (15). In fact, for unscreened haloes the fifth force has the effect to increase the velocities of particles up to a factor of $\approx\sqrt{4/3}$ with respect to standard GR for a given radial mass distribution, so that equation (15) will return a correspondingly higher value of the derived concentration parameter. Nonetheless, the determination of the concentration based on equation (15) still provides a quantitatively reliable outcome at small masses – where a suppression of concentration is found by both methods – and for the most massive haloes that are expected to be screened and therefore not affected by the velocity boost. Then, even though the profile fitting method represents the most correct procedure for the determination of the halo concentrations, we consider the comparison shown in Fig. 8 an interesting result by itself.

By analysing more in detail the results displayed in the right-hand panel of Fig. 8 – which we will consider as the reference from now on – we can see that the WDM model in standard GR shows the expected suppression of the halo concentrations at low masses and progressively recovers the standard ΛCDM result at larger masses. A maximum suppression of ≈ 25 per cent is found for the lowest masses available to our sample, while at the four largest mass bins the model is again consistent with ΛCDM at 2σ.

The CDM model within $f(R)$ gravity, instead, shows a moderate increase of halo concentrations (up to 30 per cent) for intermediate masses and recovers the standard value of the concentration–mass relation only at the highest mass bin. Interestingly, the lowest mass haloes with virial masses $M_{200} \lesssim 2 \times 10^{12}\,\mathrm{M}_\odot\,h^{-1}$ show a lower

Figure 8. The ratio of the concentration–mass relation to the standard ΛCDM case for the different cosmologies under investigation as computed through the kinetic method of equation (15) (left-hand panel) and by a full NFW profile fitting (right-hand panel). In both plots the grey-shaded regions represent the 1σ uncertainty on the ratio based on the Poisson error on the average concentration in each bin, while the blue dashed line represents the simple superposition of the separate effects of WDM (red curve) and *f(R)* gravity (green curve).

concentration compared to the standard model. This is qualitatively consistent with the behaviour of the density profiles shown in Fig. 7. Such suppression of halo concentrations has been found for a fraction of the considered haloes with masses around $2 \times 10^{12}\,M_\odot\,h^{-1}$ also in the higher resolution study of Arnold et al. (2016) and for a lower value of the *f(R)* scalar amplitude ($\bar{f}_{R0} = -10^{-6}$), while the majority of haloes did show an increased concentration. Again, a resolution comparable to Arnold et al. for a halo sample with similar statistics to our work would be required to robustly assess the impact of *f(R)* gravity on the concentrations of haloes below such mass value.

Finally, the outcomes of the combined WDM–*f(R)* cosmology show a very interesting distortion of the concentration–mass relation, again fully consistent with the results obtained for the density profiles: a weaker enhancement of halo concentrations compared to the CDM realization of *f(R)* gravity for intermediate masses with a *steeper* and *stronger* suppression of halo concentrations at low masses even when compared with the WDM cosmology for standard GR. In both plots of Fig. 8 the blue dashed line shows the simple superposition of the relative effects of WDM and *f(R)* gravity, which is found also in this case to provide a relatively good match to the outcome of the full combined simulation.

The suppression of the inner halo density – and consequently of the halo concentration – for low-mass haloes that we find for the *f(R)* cosmologies for both CDM and WDM compared to the standard GR case (Figs 7 and 8) is not easily understandable in terms of the different regimes of action of the chameleon screening mechanism and would deserve further investigation, in particular – as already stated above – a more detailed analysis based on higher resolution simulations, which we defer to future work.

4.3 Statistical and structural properties of cosmic voids

Cosmic voids have attracted significant interest in the past few years as possible complementary cosmological probes to the standard large-scale structure observables. In particular, previous investigation of the statistical and structural properties of cosmic voids in MG theories has been performed by e.g. Cai et al. (2015), while a study of the impact of WDM on cosmic voids has been presented in Yang et al. (2015).

In this work we investigate for the first time the joint effects of these two modifications of the standard cosmological model on cosmic voids, focusing in particular on the abundance and on the density profiles of relatively small voids. Although a realistic determination of the expected observational properties of cosmic voids should properly take into account the effect of the bias of the visible tracers (such as galaxies and clusters) employed to identify the voids in large cosmological surveys (see e.g. Nadathur & Hotchkiss 2015; Pollina et al. 2016), a clear understanding of the properties of cosmic voids in the underlying matter density field represents an essential step to employ voids as cosmological probes.

4.3.1 Abundance of cosmic voids

Following the discussion presented in Yang et al. (2015) we have computed the abundance of cosmic voids as a function of their core density within 30 bins spanning the range of core densities covered by our void sample – after performing the selection procedures described above in Section 3.2 – which goes from 0 to ≈0.2 in units of the mean particle density. Such distribution is in fact more representative of the average structural properties of the void population than the size distribution function, due to the unrealistic assumption of sphericity that enters the definition of the void effective radius (see again Yang et al. 2015). The resulting core density distribution functions are displayed in Fig. 9, where the error bars overplotted on the standard ΛCDM curve are 2σ errors computed as the Poissonian uncertainties associated with the number counts in each bin.

As one can see in the plot, consistently with the outcomes of Yang et al. (2015), we do find that our WDM model within standard GR (red open squares, having a WDM mass of 0.4 keV corresponding to the most extreme cut-off value considered in Yang et al. 2015) determines an overabundance of voids with higher core densities and a corresponding suppression of the abundance of the most empty voids. In this respect, we confirm the results obtained by Yang et al. (2015) with simulations of comparable resolution as ours.

The CDM realization of *f(R)* gravity (open green triangles) shows exactly the opposite behaviour, with a significant enhancement of the most empty voids and a suppression of the large core density tail of the distribution.
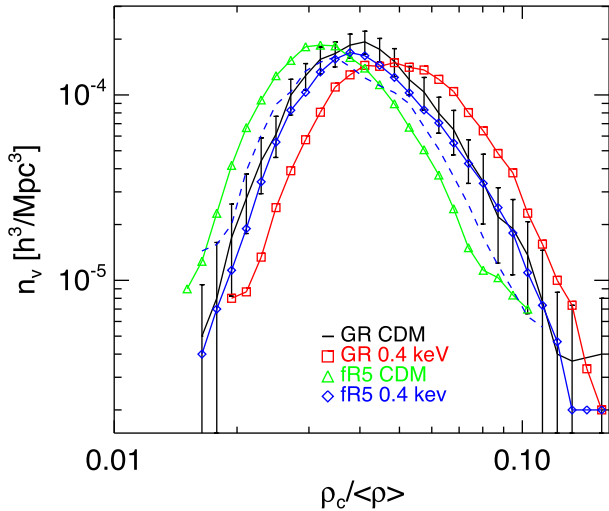
Figure 9. The differential distribution function of cosmic voids as a function of their core density (i.e. the number density n_v of voids in each core density bin) for the various cosmologies. The error bars on the reference ΛCDM model correspond to the 2σ Poissonian error on the number counts in each bin. The blue dashed curve represents the simple combination of the deviations of the two individual simulations from the standard ΛCDM case.

Quite remarkably, finally, the core density distribution function that results from the WDM model within the $f(R)$ gravity simulation shows that the effect associated with the thermal cut-off due to the low WDM particle mass is almost perfectly counterbalanced by the modified gravitational evolution, so that the resulting abundance of voids is again consistent with the standard model within statistical uncertainties. This result provides the first evidence of an intrinsic observational degeneracy between WDM and $f(R)$ gravity at the level of the statistical properties of the population of small cosmic voids.

Even though the degeneracy between these two modifications of the standard cosmological model is easily broken by a number of other observables (as we have extensively shown in the previous sections), it is interesting to notice that for objects that are only mildly non-linear (such as cosmic voids) but still at relatively small scales the two models mask each other almost perfectly. This outcome, as we will show in the next section, is not a peculiar coincidence occurring only for the core density distribution function, but appears to characterize also the structural properties of small voids, while for larger voids (arising from larger modes of the primordial density spectrum) the effect of WDM becomes less pronounced so that the expected imprint of $f(R)$ gravity stems out prominently.

4.3.2 Void density profiles

As a final test of our set of cosmological models we have computed the average void density profiles for voids with effective radius $R_{\rm eff}$ below $5\,h^{-1}$ Mpc and between 5 and $10\,h^{-1}$ Mpc, by stacking the individual spherically averaged density profiles of 100 randomly selected voids for each of these two bins of $R_{\rm eff}$. The resulting mean profiles are displayed in the left- and right-hand panels of Fig. 10, respectively. In the two plots, the top panels show the density profiles, with the error bars on the standard ΛCDM curves representing the Poissonian errors on the mean, while the bottom panels show the relative difference with respect to the standard model, with the grey-shaded regions indicating the 2σ confidence region based on a bootstrap resampling technique with 1000 resamples of the 100

individual profiles, as already done for the halo density profiles discussed in Section 4.2.3.

Consistently with Yang et al. (2015) and with the previous results on the core density distribution, we find that WDM within standard GR results in shallower density profiles for the smallest voids, while no statistically significant effect appears for somewhat larger voids.

On the contrary, the effects of $f(R)$ gravity for a standard CDM particle candidate are present for both small and larger voids, resulting in a steeper profile with a lower central density. This is consistent with previous studies on the structural properties of cosmic voids in MG cosmologies (see again Cai et al. 2015).

As a result, the density profiles for the smallest voids in the combined WDM–$f(R)$ cosmology are again fully consistent with the standard ΛCDM scenario, thereby confirming the degeneracy between these two models in the properties of cosmic voids already identified in the previous section for the core density distribution. For the larger voids, quite expectedly, the degeneracy is much weaker due to the lower impact of the WDM cut-off and the still significant effect of the scalar fifth force of the $f(R)$ MG model.

5 CONCLUSIONS

We have performed an extended analysis of two cosmological N-body simulations featuring either a WDM particle candidate or an $f(R)$ MG theory and compared their outcomes to the standard ΛCDM cosmology. This analysis has provided fully consistent results with the long series of previous works investigating the same models.

Additionally, we have presented for the first time the results of a cosmological simulation jointly including the effects of both these deviations from the ΛCDM cosmology, and tested possible degeneracies of the two independent modifications of the standard model on a wide range of large-scale structure statistics. As one would have naively expected, for most observables the joint effect of these two modifications is given by the simple superposition of the separate effects, in particular for those circumstances where these affect the observable on well distinct scales. Such behaviour can be therefore easily described in terms of the well-understood physics governing the two separate non-standard models under the assumption that the coupling between them is small. Nonetheless, this simple behaviour does not apply to all observables investigated in the present work, signalling that the assumption of a negligible contribution coming from the coupling of the two models breaks down in some specific regimes.

In particular, we have investigated the properties of the large-scale matter distribution by extracting from all our simulations the non-linear matter power spectrum both in real- and redshift space, the statistics of the halo populations within the different models and the structural properties of collapsed structures over a wide range of masses, as well as the properties of cosmic voids arising in these different cosmological scenarios. Our results have shown that most observables do not show a significant degeneracy between the effects of the WDM particle and those of a modified law of gravity, while a few other observables are indeed characterized by a strong degeneracy.

More specifically, our main results can be summarized as follows.

(i) *The matter power spectrum $P(k)$ in configuration space* shows the well-known features for the individual WDM and $f(R)$ cosmologies, i.e. a scale-dependent suppression of power below a cut-off scale $k_c \approx 2\,h\,{\rm Mpc}^{-1}$ for the former and an scale-dependent enhancement of power for the latter, both with an amplitude
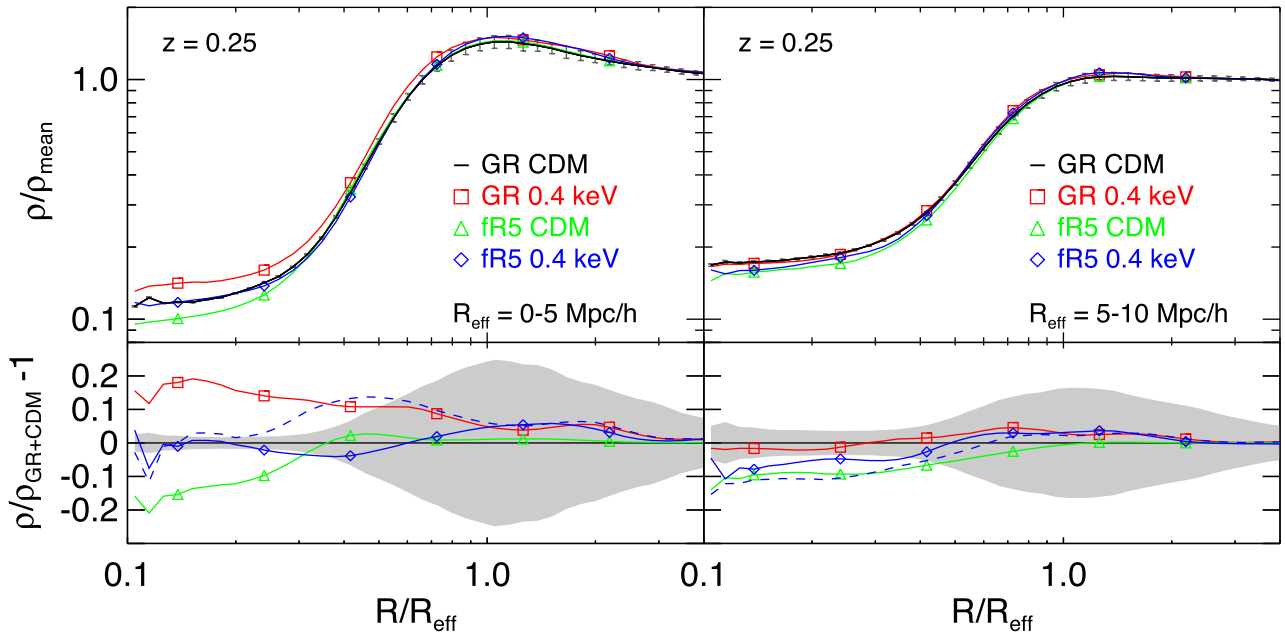
Figure 10. The stacked void density profiles in two different ranges of effective radius for the various cosmologies. The upper plots show the mean spherically averaged density profiles of 100 randomly selected voids, with the (barely visible) error bars representing the Poissonian error on the mean. The lower plots display the relative difference with respect to the standard ΛCDM cosmology with the grey-shaded regions representing the 2σ confidence region based on a bootstrap computation of the standard deviation of the average profiles. The blue dashed curve represents the combination of the deviations of the two individual simulations from the standard ΛCDM case.

increasing with scale. These effects have been widely discussed in the literature and are well understood as resulting from the primordial cut-off in the density power spectrum and from the effect of the fifth force associated with the scalar degree of freedom f_R, respectively. In particular, for the WDM simulation we find that the cut-off is well captured by the fitting formula provided by Viel et al. (2012), which provides a consistency check for our numerical integration. The combined model shows an identical behaviour as the $f(R)$ cosmology down to the cut-off scale k_c, followed by a suppression of the MG enhancement. Quite remarkably, we find that the suppression induced by WDM with respect to the CDM scenario within $f(R)$ gravity follows the same best-fitting shape obtained by the fitting formula of Viel et al. (2012) for the standard GR simulation. Therefore, our results provide the first validation of this widely used fitting formula for non-GR cosmologies.

(ii) *The matter power spectrum $P_s(k)$ in redshift space* exhibits differences among models of a maximum of $\sim$15 per cent, showing that the matter clustering properties are much more degenerate in redshift space than in real space. This demonstrates that the effect of peculiar velocities compensates the deviations that the nature of dark matter and the gravity model induce on the clustering of matter. We also find that the ratio of monopoles in redshift and real space clearly segregate models, on small scales, according to the underlying gravity model, while on large scales the amplitude and shape is very degenerate among all models.

(iii) *The halo bias $b(k)$* shows that models with WDM have a larger amplitude, on all scales, with respect to the models with CDM, independently of the underlying gravity theory. We find that on scales $k \lesssim 0.2\,h\,\mathrm{Mpc}^{-1}$ relative differences among models are scale independent and amount to $\sim$20 per cent when comparing cosmologies with the same gravitational theory. Differences in halo bias among models with the same dark matter particle mass but different gravitational theories are somewhat smaller reaching $\sim$10 per cent.

(iv) *The halo mass function* shows the well-known suppression of the abundance of small haloes for the WDM cosmology, and the expected mass-dependent enhancement of the abundance of haloes for the $f(R)$ gravity model. In this case, however, differently from the situation encountered for the matter power spectrum, the two effects have the opposite dependence on the halo mass, with the former increasing for progressively lower masses and the latter increasing for progressively larger masses. This different mass dependence ensures that no degeneracy appears when the two models are jointly at work. In fact, the low-mass range of the resulting halo mass function follows the same suppression found for the WDM model, while the high-mass range closely follows the $f(R)$ mass function. The transition between these two regimes is found to occur at $\approx 2 \times 10^{12}\,\mathrm{M_\odot}\,h^{-1}$.

(v) *The subhalo mass function* shows – for the WDM case – the expected strong suppression of the abundance of substructures, in particular for subhaloes with mass ratio to their host main structure below 10^{-2}, while no statistically significant change in the abundance of substructures is observed for the $f(R)$ gravity scenario. Then, quite expectedly, the combination of the two models substantially follows the behaviour of the WDM cosmology in standard GR with a comparable reduction of the number of small subhaloes.

(vi) *The halo density profiles*, compared among the different models through a stacking procedure of 1000 randomly selected haloes for several different halo mass bins, show a significant shallowing of the density profiles for the WDM model at small halo masses, which is progressively reduced for higher mass bins. On the contrary, the $f(R)$ model shows a more complex modulation of the deviation from the standard ΛCDM profiles, due to the different impact of the chameleon screening mechanism for different masses and overdensity environments, with very little deviations observed at the largest mass bins, and a significant steepening of the profiles for intermediate masses, while the smallest haloes show

a suppression of the inner overdensity similar – although weaker – to the WDM case. Interestingly, the combined model is found to enhance the WDM suppression of the inner halo overdensities at small masses and to reduce the $f(R)$ increase of the inner halo overdensities at intermediate masses.

(vii) *The concentration–mass relation* shows an interesting behaviour, fully consistent with the results obtained for the halo density profiles in the different mass ranges. On one hand, the WDM scenario within standard GR displays the well-known suppression of the halo concentrations for low-mass haloes, while the standard c–M relation is recovered for larger masses; on the other hand, the two $f(R)$ cosmologies for both CDM and WDM are found to provide an enhancement of halo concentrations at intermediate masses, with a peak of the deviation from ΛCDM at $\approx 10^{13}$ M$_\odot$ h^{-1}, and a suppression of concentration at the lowest masses covered by our sample, which is more pronounced for the WDM realization as compared to the CDM case. While this suppression may be expected in the former case, the deviation found for CDM in $f(R)$ gravity represents an interesting feature deserving further investigation with higher resolution simulations.

(viii) *The abundance of cosmic voids* is found to be one of the few observables (together with the matter power spectrum in redshift space discussed above and with the void profiles summarized below) for which WDM and $f(R)$ gravity show a significant degeneracy. In particular, as already found by Yang et al. (2015), WDM determines a suppression of the abundance of small voids with core density below 5 per cent of the mean cosmic density, and a corresponding enhancement of the abundance of voids above this threshold. This corresponds to voids being less underdense in WDM compared to CDM. On the other hand, $f(R)$ gravity is found to determine the opposite effect on the population of small cosmic voids, with an enhancement of the abundance of the most underdense voids and a corresponding suppression of the less underdense ones. As a result, the combined cosmology featuring both WDM and $f(R)$ gravity shows a very strong degeneracy with the standard ΛCDM result, with the core density distribution function being consistent with the standard model at 2σ confidence level.

(viii) *The density profiles of cosmic voids* show a different range of effects for the different cosmologies depending on the void size. For small voids ($R_{\rm eff} \leq 5\ h^{-1}$ Mpc) WDM is found to make the void profiles shallower, with an inner density about 20 per cent larger than in the standard ΛCDM model, consistently with the previous results of Yang et al. (2015), while for larger voids ($5 < R_{\rm eff} \leq 10\ h^{-1}$ Mpc) the impact of WDM is very mild, with the density profiles consistent at 2σ with the standard scenario. On the other hand, $f(R)$ gravity has the opposite effect of steepening the void profiles on both ranges of void size, even though the amplitude of the suppression of the inner void density is more pronounced for the smallest voids. As a result, the combined model featuring at the same time WDM and $f(R)$ gravity is strongly degenerate with ΛCDM for the smallest voids while resulting marginally distinguishable from the standard model for the larger ones. In this respect, we have extended the results of Yang et al. (2015) to the case of a non-standard theory of gravity, finding evidence of a strong degeneracy between the two models in the observables where the signatures of WDM first identified by Yang et al. (2015) are more pronounced.

To summarize, we have performed and presented in this paper – for the first time – the results of a cosmological simulation of structure formation for a WDM particle candidate evolving under the effect of a modified theory of gravity, and compared its results to the reference ΛCDM cosmology and to the separate effects of these two modifications of the standard cosmology.

We have performed an extensive analysis of the simulated matter distribution and of the properties of the resulting linear and non-linear structures, including haloes, subhaloes and voids, and identified possible observational degeneracies between the models. We found that – differently from the case of cosmologies featuring simultaneously MG and massive neutrinos discussed in Baldi et al. (2014), for a more restricted range of observables – most of the standard statistics do not show any significant degeneracy due to the fact that WDM and $f(R)$ gravity impact these statistics with very different functional dependencies on cosmic scales and halo masses.

However, we also found that a clear degeneracy exists in the observational properties of small cosmic voids, with both their abundance and their density profiles being hardly distinguishable in the combined WDM–$f(R)$ simulation from the corresponding results in the standard ΛCDM cosmology, even if the two models show – individually – a clear and distinctive signature in these observables.

ACKNOWLEDGEMENTS

REFERENCES

Achitouv I., Baldi M., Puchwein E., Weller J., 2016, Phys. Rev. D, 93, 103522

Alam S. et al., 2017, MNRAS, 470, 2617

Angulo R. E., Hahn O., Abel T., 2013, MNRAS, 434, 3337

Arnold C., Puchwein E., Springel V., 2014, MNRAS, 440, 833

Arnold C., Puchwein E., Springel V., 2015, MNRAS, 448, 2275

Arnold C., Springel V., Puchwein E., 2016, MNRAS, 462, 1530

Avila-Reese V., Colin P., Valenzuela O., D'Onghia E., Firmani C., 2001, ApJ, 559, 516

Baldi M., Villaescusa-Navarro F., Viel M., Puchwein E., Springel V., Moscardini L., 2014, MNRAS, 440, 75

Bertotti B., Iess L., Tortora P., 2003, Nature, 425, 374

Blake C. et al., 2011, MNRAS, 415, 2876

Bode P., Ostriker J. P., Turok N., 2001, ApJ, 556, 93

Boylan-Kolchin M., Bullock J. S., Kaplinghat M., 2011, MNRAS, 415, L40

Boylan-Kolchin M., Bullock J. S., Kaplinghat M., 2012, MNRAS, 422, 1203

Cai Y.-C., Li B., Cole S., Frenk C. S., Neyrinck M., 2014, MNRAS, 439, 2978

Cai Y.-C., Padilla N., Li B., 2015, MNRAS, 451, 1036

Carucci I. P., Villaescusa-Navarro F., Viel M., Lapi A., 2015, J. Cosmol. Astropart. Phys., 07, 047

Colín P., Avila-Reese V., Valenzuela O., 2000, ApJ, 542, 622

Davis M., Efstathiou G., Frenk C. S., White S. D., 1985, ApJ, 292, 371

Delubac T. et al., 2015, A&A, 574, A59

Dunstan R. M., Abazajian K. N., Polisensky E., Ricotti M., 2011, preprint (arXiv:1109.6291)

Fontanot F., Puchwein E., Springel V., Bianchi D., 2013, MNRAS, 436, 2672

Gilmore G., Wilkinson M. I., Wyse R. F. G., Kleyna J. T., Koch A., Evans N. W., Grebel E. K., 2007, ApJ, 663, 948

Gronke M., Mota D. F., Winther H. A., 2015, A&A, 583, A123

Hansen S. H., Lesgourgues J., Pastor S., Silk J., 2002, MNRAS, 333, 544

Hellwing W. A., Barreira A., Frenk C. S., Li B., Cole S., 2014, Phys. Rev. Lett., 112, 221102

Heymans C. et al., 2013, MNRAS, 432, 2433

Hildebrandt H. et al., 2017, MNRAS, 465, 1454

Hu W., Sawicki I., 2007, Phys. Rev. D, 76, 064004

Hu B., Raveri M., Frusciante N., Silvestri A., 2014, Phys. Rev. D, 89, 103530

Hu B., Raveri M., Rizzato M., Silvestri A., 2016, MNRAS, 459, 3880

Inoue K. T., Takahashi R., Takahashi T., Ishiyama T., 2015, MNRAS, 448, 2704

Jain B., VanderPlas J., 2011, J. Cosmol. Astropart. Phys., 10, 032

Jain B., Vikram V., Sakstein J., 2013, ApJ, 779, 39

Jennings E., Baugh C. M., Li B., Zhao G.-B., Koyama K., 2012, MNRAS, 425, 2128

Kennedy R., Frenk C., Cole S., Benson A., 2014, MNRAS, 442, 2487

Khoury J., Weltman A., 2004, Phys. Rev. D, 69, 044026

Klypin A. A., Kravtsov A. V., Valenzuela O., Prada F., 1999, ApJ, 522, 82

Kuzio de Naray R., Martinez G. D., Bullock J. S., Kaplinghat M., 2010, ApJ, 710, L161

Li B., Zhao G.-B., Koyama K., 2012, MNRAS, 421, 3481

Li B., Zhao G.-B., Teyssier R., Koyama K., 2012, J. Cosmol. Astropart. Phys., 01, 051

Li B., Hellwing W. A., Koyama K., Zhao G.-B., Jennings E., Baugh C. M., 2013, MNRAS, 428, 743

Llinares C., Mota D. F., Winther H. A., 2014, A&A, 562, A78

Lombriser L., 2014, Ann. Phys., 526, 259

Lombriser L., Li B., Koyama K., Zhao G.-B., 2013, Phys. Rev. D, 87, 123511

Lombriser L., Koyama K., Li B., 2014, J. Cosmol. Astropart. Phys., 03, 021

Lovell M. R. et al., 2012, MNRAS, 420, 2318

Maccio A. V., Paduroiu S., Anderhalden D., Schneider A., Moore B., 2012, MNRAS, 424, 1105

Maio U., Viel M., 2015, MNRAS, 446, 2760

Markovic K., Bridle S., Slosar A., Weller J., 2011, J. Cosmol. Astropart. Phys., 01, 022

Mead A. J., Heymans C., Lombriser L., Peacock J. A., Steele O. I., Winther H. A., 2016, MNRAS, 459, 1468

Miranda M., Maccio A. V., 2007, MNRAS, 382, 1225

Moore B., Ghigna S., Governato F., Lake G., Quinn T., Stadel J., Tozzi P., 1999, ApJ, 524, L19

Nadathur S., Hotchkiss S., 2015, MNRAS, 454, 889

Narayanan V. K., Spergel D. N., Dave R., Ma C.-P., 2000, ApJ, 543, L103

Navarro J. F., Frenk C. S., White S. D. M., 1997, ApJ, 490, 493

Neyrinck M. C., 2008, MNRAS, 386, 2101

Oyaizu H., Lima M., Hu W., 2008, Phys. Rev. D, 78, 123524

Perlmutter S. et al., 1999, ApJ, 517, 565

Planck Collaboration XVI, 2014, A&A, 571, A16

Planck Collaboration XXIV, 2016, A&A, 594, A24

Planck Collaboration XIII, 2016, A&A, 594, A13

Platen E., van de Weygaert R., Jones B. J. T., 2007, MNRAS, 380, 551

Pogosian L., Silvestri A., 2008, Phys. Rev. D, 77, 023503

Pollina G., Baldi M., Marulli F., Moscardini L., 2016, MNRAS, 455, 3075

Puchwein E., Baldi M., Springel V., 2013, MNRAS, 436, 348

Reid B. A. et al., 2012, MNRAS, 426, 2719

Riess A. G. et al., 1998, AJ, 116, 1009

Salucci P., Lapi A., Tonini C., Gentile G., Yegorova I., Klein U., 2007, MNRAS, 378, 41

Schmidt F., 2010, Phys. Rev. D, 81, 103002

Schmidt B. P. et al., 1998, ApJ, 507, 46

Schmidt F., Lima M. V., Oyaizu H., Hu W., 2009, Phys. Rev. D, 79, 083518

Schneider A., Smith R. E., Maccio A. V., Moore B., 2012, MNRAS, 424, 684

Schultz C., Oñorbe J., Abazajian K. N., Bullock J. S., 2014, MNRAS, 442, 1597

Simpson F. et al., 2016, Phys. Rev. D, 93, 023525

Springel V., White S. D. M., Tormen G., Kauffmann G., 2001, MNRAS, 328, 726

Springel V. et al., 2008, MNRAS, 391, 1685

Sutter P. M. et al., 2015, Astron. Comput., 9, 1

van Eymeren J., Trachternach C., Koribalski B. S., Dettmar R.-J., 2009, A&A, 505, 1

Viel M., Lesgourgues J., Haehnelt M. G., Matarrese S., Riotto A., 2005, Phys. Rev. D, 71, 063534

Viel M., Markovic K., Baldi M., Weller J., 2012, MNRAS, 421, 50

Viel M., Becker G. D., Bolton J. S., Haehnelt M. G., 2013, Phys. Rev. D, 88, 043502

Vikhlinin A. et al., 2009, ApJ, 692, 1060

Vikram V., Cabré A., Jain B., VanderPlas J. T., 2013, J. Cosmol. Astropart. Phys., 08, 020

Villaescusa-Navarro F., Dalal N., 2011, J. Cosmol. Astropart. Phys., 03, 024

Walker M. G., Peñarrubia J., 2011, ApJ, 742, 20

Wang J., White S. D. M., 2007, MNRAS, 380, 93

Will C. M., 2005, Living Rev. Relativ., 9, 3

Winther H. A. et al., 2015, MNRAS, 454, 4208

Yang L. F., Neyrinck M. C., Aragón-Calvo M. A., Falck B., Silk J., 2015, MNRAS, 451, 3606

Yoshida N., Sokasian A., Hernquist L., Springel V., 2003, ApJ, 591, L1

Zel'dovich Y. B., 1970, A&A, 5, 84

This paper has been typeset from a TeX/LaTeX file prepared by the author.